Journal of Civil Structural Health Monitoring (2026) 16:54
https://doi.org/10.1007/s13349-026-01086-1

ORIGINAL PAPER

UAV-mounted single-beam sonar for rapid bathymetric monitoring of coastal infrastructure: implications for structural health assessment

Bethsaide Souza-Santos[1,2] · **Marcos Arza-García**[1] · **Juan Ortiz-Sanz**[1] · **Mariluz Gil-Docampo**[1]

Received: 24 September 2025 / Revised: 20 December 2025 / Accepted: 22 June 2026
© The Author(s) 2026

Abstract

Accurate bathymetric data are essential for the design and monitoring of coastal structures, but conventional multibeam surveys are costly and often impractical in shallow or confined areas. We evaluate a single-beam echosounder (SBES, ECT400) suspended beneath an unmanned aerial vehicle (UAV) as a rapid method with low logistical requirements for bathymetric monitoring of coastal infrastructure. Fieldwork was performed in an operational dry dock that was alternately drained and filled, enabling direct geometric validation against an ultra-high-resolution photogrammetric DEM (0.55 cm GSD). The co-registered dataset comprises N = 16,137 sonar returns to depths of ≈ 8 m. The UAV-mounted SBES produced a mean depth difference of 0.15 m (SD = 0.58 m) relative to the photogrammetric reference. From these residuals we estimate a 95% Minimum Detectable Change (MDC_{95}) of ≈ 0.5 m when changes are assessed by aggregating repeated co-located passes. These results indicate that the UAV-SBES workflow is suitable as a Tier-1 screening tool for structural-health monitoring, effective for detecting metre- to decimetre-scale changes and triaging sites for targeted high-precision follow-up, but not for micrometre/mm-scale deformation monitoring. The method's portability and vessel-free operation make it especially useful for frequent inspections in shallow, confined coastal settings.

Keywords Structural health monitoring · UAV bathymetry · Single-beam echosounder (SBES) · Photogrammetry · Coastal infrastructure · Change detection

Abbreviations

ASV	Autonomous surface vehicle
COTS	Commercial off-the-shelf
CSV	Comma-separated values
DAP-UAV	Digital Aerial Photogrammetry (UAV)
DEM	Digital elevation model
ECT400	Echologger ECT400 (device model)
GCP	Ground Control Point
GeoTIFF	GeoTIFF (georeferenced TIFF format)
GNSS	Global Navigation Satellite System
GSD	Ground sampling distance
IHO	International Hydrographic Organization
LiDAR	Light detection and ranging
MDC_{95}	Minimum detectable change at 95% confidence
MBES	Multibeam echosounder
RMSE	Root mean square error
RTK	Real-time kinematic
SBES	Single-beam echosounder
SD	Standard deviation
SHM	Structural health monitoring
SkyHub	Product name for SBES + GPS logging/synchronization
UAV	Unmanned aerial vehicle
USV	Uncrewed surface vehicle
XYZ	Cartesian coordinates (x, y, z)

✉ Bethsaide Souza-Santos
bethsaide.souza@rai.usc.gal

Marcos Arza-García
m.arza@usc.es

Juan Ortiz-Sanz
juan.ortiz@usc.es

Mariluz Gil-Docampo
ml.gil@usc.es

1 Department of Agroforestry Engineering, Higher Polytechnic Engineering School, University of Santiago de Compostela, Santiago de Compostela, Spain

2 Departamento de Tecnologia, Universidade Estadual de Feira de Santana, Feira de Santana, Brazil

Published online: 21 July 2026

1 Introduction

Reliable bathymetric measurements are essential in coastal engineering for the design, construction, risk management and maintenance of maritime structures such as docks, breakwaters, tidal channels, and harbours. Bathymetry also underpins broader coastal applications including sediment-transport modelling [1], marine ecological studies [2], dredging operations planning [3], and shoreline change analysis [4]. Techniques like airborne Light Detection and Ranging (LiDAR) [5, 6] and satellite-derived bathymetry [7, 8] have recently expanded data acquisition options, particularly in large shallow coastal areas. However, precise bathymetric surveys still predominantly rely on multibeam echosounder systems (MBES), which can achieve sub-5 cm vertical accuracy [9, 10] but require expensive sensors, specialized survey vessels, trained operators, and complex post-processing workflows. This combination of logistical and financial constraints often limits their feasibility in confined, shallow, or otherwise difficult-to-access environments, making conventional methods inaccessible for small-scale projects or rapid assessments where dedicated resources are unavailable.

In such confined or difficult-to-access environments, advances in unmanned platforms, both aerial (UAV) and surface-based (USV/ASV), have significantly expanded the available toolkit for bathymetric mapping [11]. Recent studies have explored their integration with different sensors, including single-beam echosounders (SBES), which range from survey-grade systems to devices originally designed for recreational fishing [12]. For instance, [13] presented a tethered boat system equipped with a Commercial Off the Shelf (COTS) chirp/sidescan sonar for mapping small water bodies (< 3 m depth). Furthermore, mounting SBES on UAVs enables surveys in areas inaccessible to boats and offers new possibilities for rapid and flexible bathymetric data collection [14].

Most existing research on SBES focuses on characterization of seabed sediments or acoustic backscatter rather than on their geometric accuracy relative to external reference datasets. For example, Mopin Famiglietti [15] developed a multi-frequency SBES capable of generating non-linear harmonics to resolve phase ambiguities and derive sediment properties, while Ri et al. [16] applied neural networks to classify riverbed sediment roughness and hardness. Gogendeau et al. [17] integrated SBES with USV and photogrammetry sensors for ecological monitoring, validating depths to International Hydrographic Organization (IHO) Order 1a standards but focusing on multi-sensor data fusion rather than geometric accuracy per se. Recent work has demonstrated the effectiveness of UAV-based photogrammetry combined with deep-learning methods for semi-autonomous inspection of concrete structures [18] and crack detection for building damage inspections [19], highlighting the value of high-resolution aerial imagery in structural health assessment.

However, when assessing the geometric accuracy of these SBES systems, most comparative studies rely on references such as MBES or airborne LiDAR bathymetry [20, 21]. While these approaches are widely accepted, they are also affected by limitations inherent to acoustic or optical propagation in the water column, such as turbidity, scattering, and variable sound speed profiles, which may propagate systematic errors into validation datasets [22–24].

Very few studies have attempted to evaluate SBES precision against direct topographic measurements unaffected by water column uncertainties. For instance, Tuno [25] validated SBES measurements in a marina against total station observations using a long rod (> 4 m), achieving a Root Mean Squared Error (RMSE) of 0.17 m up to 4.3 m depth. Although this demonstrated the viability of SBES in shallow waters, their study was limited in depth range and environmental conditions. Similarly, in their second case study, Bandini [14] evaluated SBES precision by comparing tethered sonar measurements with ground truth depths obtained using a weighted tape line (with an accuracy of approximately 10–15 cm up to 40 m depth) and reported final errors around 2.1% of actual depth.

Due to the scarcity of such field-based geometric accuracy assessments, and the inherent complexity of conducting them under real conditions, some authors have proposed simulation-based calibration approaches as practical alternatives. Chen et al. [26] developed an equivalent electronic measurement method to simulate acoustic propagation in laboratory settings without requiring large tanks, enabling controlled verification of sonar response across different depths. Similarly, Kartal et al. [27] modelled bottom inclination and beam angle errors using simulated SBES data collected from a small surface vehicle, aiming to improve depth correction algorithms without the logistical challenges of extensive field campaigns.

In this context, the present study evaluates the performance of a UAV-mounted SBES within a large operational dry dock used by the Spanish Navy. Uniquely, the dock's fill-and-drain capability enabled direct validation of underwater sonar measurements against an aerial photogrammetric digital model of the dry dock floor, eliminating sediment accumulation or bottom variability between datasets. This test field provided controlled conditions rarely available for such validations and allowed assessments at depths up to ~ 15 m, expanding relevance to typical coastal infrastructure applications. The approach integrates dense, uniform, high-resolution photogrammetric data with sonar-based bathymetric mapping in a controlled environment rarely used for such validations.

Previous UAV-SBES studies were carried out in natural test sites (e.g., Famiglietti et al. [28]) or validated against sparse point measurements [14], which constrains their ability to assess geometric accuracy for engineered coastal infrastructure. In contrast, our study validates sonar-derived depths in an operational dry dock that was alternately drained and filled, enabling direct comparison with an ultra-high-resolution photogrammetric Digital Elevation Model (DEM) at a Ground Sample Distance (GSD) of 0.55 cm. This approach produced a dense, co-registered dataset (N = 16,137) across depths up to ~ 15 m and allows an objective evaluation of vertical accuracy and repeatability. Testing in a constructed engineering environment reproduces the geometric complexity of coastal assets (stepped walls, structural supports and confined geometry), posing challenges for acoustic surveys that are under-represented in previous UAV-SBES validations.

The primary contribution of this work is a systematic assessment of the geometric accuracy and operational feasibility of a UAV-integrated SBES system for rapid bathymetric mapping of coastal infrastructure. To achieve this, we compared drone-mounted sonar measurements with a photogrammetric reference DEM generated from imagery with an ultra-high ground resolution of 0.55 cm, unaffected by water column distortions, enabling an objective assessment of system accuracy within the controlled dock environment.

2 Materials and methods

2.1 Study site

The study was conducted at San Julián Dock, an operational dry dock located in Ferrol, Spain (Fig. 1). This masonry structure, constructed between 1873 and 1879, measures approximately 133.4 m in length, 26.8 m in maximum width, and 16.35 m in depth, with a draft capacity of up to 10 m at high tide, enabling the servicing of vessels up to 10,000 tons [29]. Its granite composition and ability to be completely drained make it an ideal site for comparative bathymetric studies. Initially surveyed in dry conditions

Fig. 1 Study dock at the experimental site showing drained and filled conditions. **a** Dock fully drained prior to filling; **b**–**c** filling process showing the inflow jet and increasing water level; **d** dock fully filled prior to acoustic survey. Photos taken during the field campaign. Photo credit: authors

Table 1 RGB sensor parameters of the DJI M3E

Sensor type	CMOS
Sensor (mm)	17.3 × 13
Pixels	5280 × 3956
Resolution (MP)	20
Pixel size (mm)	0.00328 × 0.00328
Focal length (mm)	12.5
35 mm equivalent Focal distance (mm)	24

via UAV photogrammetry, the dock was subsequently filled with water to facilitate bathymetric data collection under controlled environmental conditions. Its dimensions and structural features make it representative of typical coastal infrastructures, enabling method validation under realistic engineering conditions.

2.2 Equipment and software

Bathymetric data were collected using an ECT400 SBES (Echologger Ltd., Seoul, South Korea) suspended beneath a DJI Matrice 300 RTK UAV (DJI, Shenzhen, China), interfaced via a SkyHub onboard computer (Fig. S1—Supplementary material) (SPH Engineering, 2024). The ECT400 operates at 450 kHz with a 5° conical beam and integrated tilt sensor, enabling precise depth measurements in shallow water environments. The UAV provides real-time kinematic positioning (RTK) with dual GNSS antennas, ensuring accurate georeferencing of sonar data and stable flight control.

The echo sounder used has a cone beam with a nominal aperture of 5° (− 3 dB) and an integrated (dual-axis) inclinometer with a tilt accuracy specified by the manufacturer of ± 0.1°. For the 5° aperture used in this work, the footprint typically varies from ≈ 0.01 m at very shallow depths to ≈ 0.60 m at the deepest point of the test.

For photogrammetric image acquisition, a DJI Mavic 3 Enterprise (M3E) UAV equipped with a fixed RGB camera was used, capturing high-resolution images for further processing using Digital Aerial Photogrammetry (DAP) and the Structure-from-Motion (SfM) technique. The RGB sensor settings are listed in Table 1.

To ensure geospatial accuracy, coordinates of 27 ground control points (GCPs) were collected using a Stonex S900T GNSS receiver (Stonex, Pavia, Italy), and photogrammetric processing was performed in Agisoft Metashape 2.0.3 Professional (Agisoft LLC, St. Petersburg, Russia). For monitoring applications, we emphasise repeatability: transects were planned to provide consistent spatial coverage and the GNSS-surveyed GCPs were used for robust co-registration; the observed agreement with photogrammetry defines the practical resolution for change detection using this workflow.

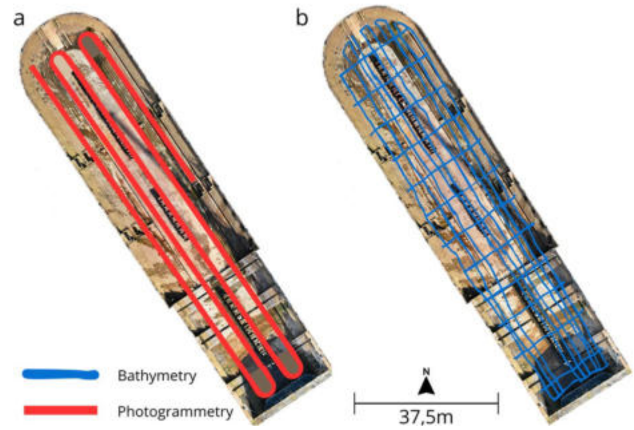

Fig. 2 UAV flight paths used for data acquisition. **a** photogrammetric survey and **b** bathymetric survey. The red tracks represent photogrammetric flight lines, while the blue tracks indicate bathymetric transects

2.3 Data collection

For bathymetric data collection, the drone flight carrying the echosounder was conducted manually due to the associated risks, and the flight lines are shown in Fig. 2b. Measurements were made with the submerged echo sounder. The SkyHub (SPH Engineering, 2024) supplies power and handles serial communication with the echosounder, connecting to the Matrice 300 RTK via the Software Development Kit (SDK) port to enable custom parameter exchange and telemetry. During the flight, the echosounder recorded real-time backscatter data along the water column.

From the telemetry log, we extracted operational statistics for the campaign. The average speed recorded during the passes was 0.99 m s^{-1} (≈ 3.56 km h^{-1}). Assuming an echo sounder ping rate of 10 Hz (equipment specification), the theoretical average spacing between echoes along the flight direction is ≈ 0.10 m, ensuring high sampling density along the transects. The flight height above the water surface, estimated from the UAV altimeter, averaged 2.05 m (σ ≈ 0.1–0.2 m). The transducer submersion relative to the surface was maintained at approximately 0.10 m (operational configuration and verified by images/telemetry). The elevation of the water surface at the dock, reported in ellipsoidal coordinates (WGS84), was 56.53 m.

To ensure accurate RTK corrections during bathymetric data acquisition, the DJI base station was positioned precisely at a location whose coordinates had been measured beforehand using the S900T GNSS receiver connected to the IGN (Instituto Geográfico Nacional) reference network. This procedure ensured that the UAV's RTK positioning was tied to an absolute geodetic reference frame, aligning the bathymetric and photogrammetric datasets within a consistent vertical datum.

The positions logged by the UAV are given in geographic coordinates referenced to WGS84, with any necessary projection conversions performed afterward. Through the link between the echosounder, SkyHub, and the Matrice 300 RTK, the onboard computer retrieves telemetry data and synchronizes it with the sonar readings in real time. These combined data include timestamped depth measurements, precise UAV positions, and relevant sensor metadata, and are saved directly onto the SkyHub as structured text files. Importantly, these files also record measurements such as the tilt angle of the sonar and the length of the suspension cable, which allows the post-processing software to compensate for sensor inclination and offset when calculating true depths. During post-processing, the files are imported into Hydromagic 7.4 (Hydromagic Software BV, Alkmaar, The Netherlands), where each sonar measurement is georeferenced using the UAV positional data and adjusted for these tilt and cable length corrections. Hydromagic then applies additional filtering as needed, producing final outputs such as georeferenced point clouds, depth profiles, and gridded bathymetric surfaces ready for analysis.

Photogrammetric data acquisition with the Mavic 3 Enterprise (DJI, Shenzhen, China) was carried out in automatic flight mode under clear, sunny conditions, which ensured good image visibility. The flight lines are shown in Fig. 2a.

The flight configuration, covering parameters such as image overlap and flight altitude, was carefully planned to ensure data quality and is summarized in Table 2. Forward overlap was set to 80% and lateral overlap to 60%, yielding a ground sampling distance (GSD) of approximately 0.55 cm/pixel. The drone maintained an altitude of 20 m during the survey, providing sufficient coverage of the dock and capturing fine details of its elevation and structural characteristics.

Additionally, 16-bit Coded Targets (Fig. S2—Supplementary material), which are artificial markers with a unique and distinct design, were placed in the scene to facilitate the automatic identification of camera positions by the software. A total of 243 images were generated, serving as the foundation for subsequent 3D modelling.

To facilitate the reproduction of the experimental protocol and clarify the integrated processing of the two datasets, Fig. 3 presents a flowchart of the workflow adopted in this study. The diagram summarizes the parallel steps of aerial photogrammetry and UAV-mounted SBES bathymetry, through sonar recording and processing, up to the georeferenced ping file.

The main outputs are co-recorded and subjected to an integrated statistical analysis that includes residual calculation (Δz), descriptive statistics, and the estimation of the Minimum Detectable Change at the 95% level (MDC_{95}).

Table 2 UAV flight parameters

Parameter	Value
Average flight speed (m/s)	2.15
Flight altitude (m)	20.00
GSD (cm/pixel)	0.55
Width of image (m)	15.6
Height of image (m)	11.7

2.4 Operational constraints and platform integration

The UAV-SBES workflow used in this study is subject to practical constraints that affect mission planning and data quality. Important factors include the UAV payload capacity and centre-of-gravity limits, flight endurance under the actual mass and aerodynamic drag of the sonar + mounting + cabling, and the effect of wind and precipitation on flight stability. In our configuration the SBES transducer was connected by a physical cable to the SkyHub onboard computer; acoustic returns were recorded locally on the onboard logger rather than relying on a continuous wireless telemetry stream for raw sonar data. Consequently, RF interference has a limited direct effect on the raw acoustic record; however, cable routing, strain relief, connector waterproofing and the mechanical pendulum behaviour of a suspended transducer must be carefully managed because they influence transducer attitude and introduce motion-induced range errors. High relative humidity and precipitation pose electrical and corrosion risks to connectors and must be mitigated with appropriate sealing and maintenance.

Prior to routine deployment we recommend (and followed for the trials reported here) a formal payload and endurance assessment (mass budget, CG check, and test flights with the full rig), verification of safe operating wind/gust limits for the platform and payload configuration, and robust mechanical fixation and strain-relief for the transducer cable. Detailed manufacturer limits for the UAV and the sonar should guide final operational envelopes.

2.5 Processing bathymetric data

The bathymetric DEM was generated from the depth points collected by the SBES, yielding a georeferenced three-dimensional (X, Y, Z) point cloud representing the underwater topography of the study area. During the survey, the echosounder recorded approximately 24,000 discrete depth measurements along multiple parallel and cross-track passes, forming a grid-like pattern with both longitudinal transects and transverse profiles over the water surface.

Prior to interpolation, the raw depth data underwent a three-step filtering process to enhance data quality:

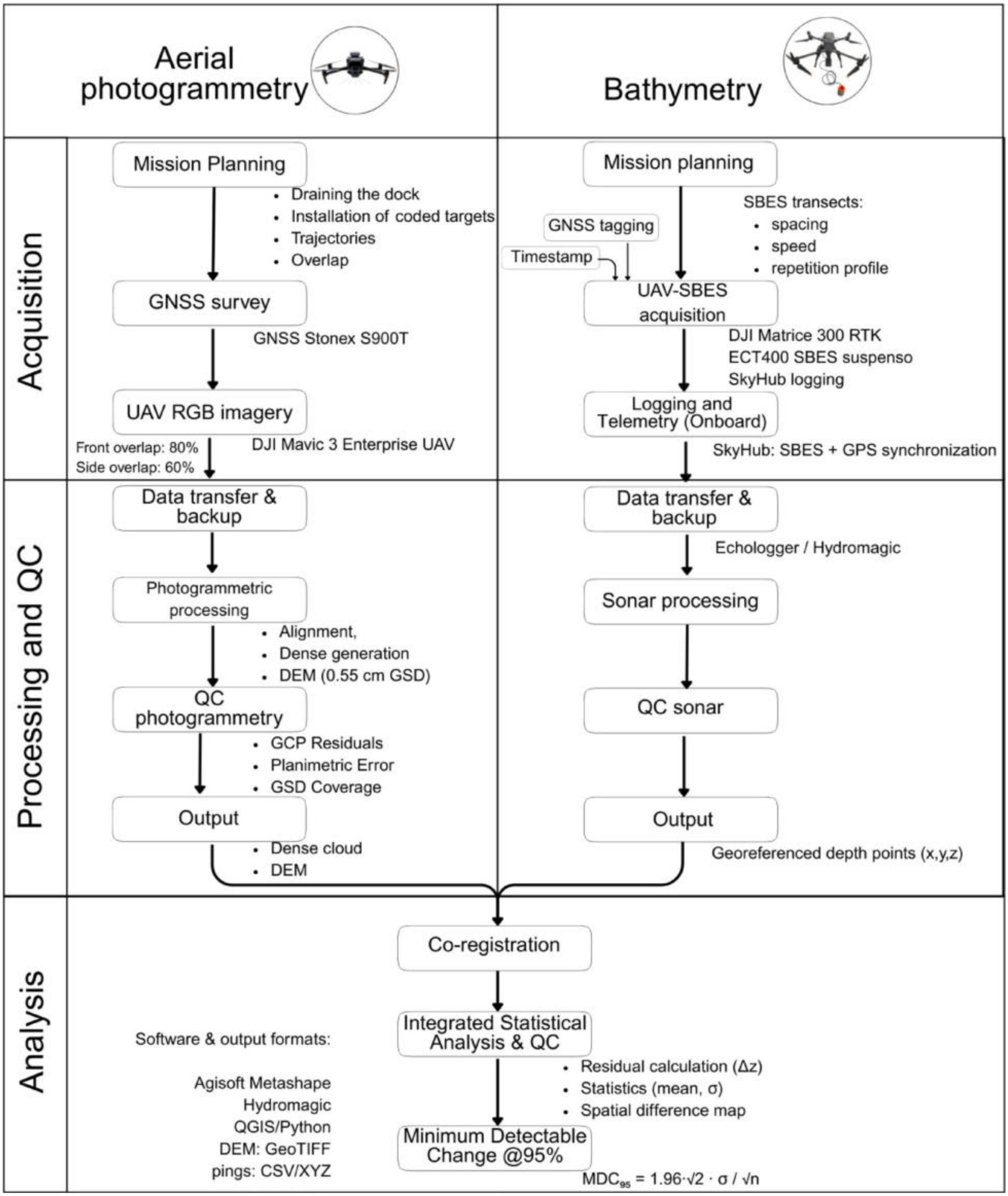

Fig. 3 Workflow summarising aerial photogrammetry and UAV-SBES bathymetry acquisition and processing steps

1. Positioning outlier removal: any points recorded with RTK disabled were automatically flagged as unreliable and excluded.
2. Statistical filtering: a three-sigma rule was applied, discarding all points whose depth deviated by more than three standard deviations from the mean, thereby minimizing the influence of outliers.
3. Physical consistency check: points inconsistent with known bathymetric constraints (e.g., negative depths or implausible abrupt changes) were removed to ensure morphological validity.

Clean sonar returns were interpolated to a regular grid using the inverse distance weighting (IDW) method. Although IDW can be suboptimal in highly variable bathymetries, it was selected here for its deterministic behaviour, computational efficiency, and minimal parameter adjustment, desirable attributes for Level 1 operational and repeatable workflows. We performed preliminary sensitivity analyses on representative subsets of the survey data, varying the power parameter (p) and the number of neighbours. In IDW, the estimated depth $\hat{z}\left(x_0\right)$ at an unsampled location x_0 is computed as a weighted average of neighbouring depths $z(x_1)$:

$$\hat{z}\left(x_0\right) = \frac{\sum_{i=1}^{n} w_i z(x_i)}{\sum_{i=1}^{n} w_i}$$

$$w_i = \frac{1}{d_i^2}$$

where $\hat{z}\left(x_0\right)$ = interpolated depth at location x_0 [m], $z(x_i)$ = measured depth at neighbour point x_i [m], d_i = distance between x_0 and x_i [m].

Here, we set the power parameter (p) to 2 and included the 12 nearest neighbours in the search radius. These parameters were chosen based on preliminary sensitivity analyses to balance interpolation smoothness and preservation of morphological detail. The resulting continuous raster DEM was exported as a GeoTIFF, capturing depth variations across the entire study area, including unsampled zones.

To assess vertical accuracy, the bathymetric DEM was compared against a high-precision UAV-derived photogrammetric DEM. Mean deviation and RMSE metrics were calculated to quantify the agreement between the two surfaces, providing an objective evaluation of echosounder performance under varying morphological conditions within the dock environment.

$$RMSE = \sqrt{\frac{1}{n}\sum_{i=1}^{n}\left(z_i^{sonar} - z_i^{photo}\right)^2}$$

where z_i^{sonar} = depth measured by the sonar [m], z_i^{photo} = depth derived from UAV photogrammetry [m], n = number of paired observations.

To translate the measured uncertainty into operational monitoring criteria, we calculated the MDC_{95} from the standard deviation σ of the vertical residuals. Considering that changes are detected by comparing means of colocalized samples between two surveys, the variance of the difference of means incorporates contributions from both measurements. Thus, for m samples aggregated by location, the standard error of the difference is $\sqrt{2}\cdot\sigma/\sqrt{m}$ and the MDC_{95} is given by:

$$MDC_{95} = z_{0.975} \cdot \sqrt{2} \cdot \frac{\sigma}{\sqrt{m}}$$

where $z_{0.975}$ = 1.96 (critical normal value for 95% confidence).

2.6 Processing photogrammetry data

Photogrammetric data processing was carried out using Agisoft Metashape 2.0.3 Professional (64-bit) software (Agisoft LLC, 2020). First, the captured high-quality images were aligned by applying internal orientation parameters and lens distortion coefficients. During this alignment phase, homologous keypoints were identified across multiple overlapping photographs, enabling precise estimation of camera positions and refinement of calibration parameters. This process resulted in a set of camera positions and a tie-point cloud, essential for generating the depth model (Fig. S3—Supplementary material).

Following image alignment, the coordinates of 27 GCP, recorded with the S900T GNSS receiver, were automatically imported and visually verified before incorporation into the reference system; 24 of these coordinates were used to scale and georeference the model, while the remaining three served as independent checkpoints for accuracy assessment. Subsequently, a high-quality dense point cloud was generated and processed using the Moderate filter setting, an intermediate noise reduction option within Metashape. This intermediate setting removes outlier points and small spurious artefacts caused by image noise or poor texture, while preserving fine structural details and sharp edges. From the filtered point cloud, a triangular mesh, a 3D model, and ultimately a DEM were derived. Lastly, the photogrammetric model's accuracy was evaluated by calculating the mean error and standard deviation of the XYZ coordinates at the three checkpoint locations.

These performance metrics provide a benchmark for defining screening thresholds in routine Structural Health

Table 3 Mean error, standard deviation, and RMSE of GCPs in DAP-UAV photogrammetric processing

	Mean error	SD of error	RMSE
X-axis (cm)	− 0.22	0.62	0.55
Y-axis (cm)	− 2.15	0.98	2.30
Z-axis (cm)	0.53	1.53	1.36
Image reprojection (pixels)	0.55	0.04	–

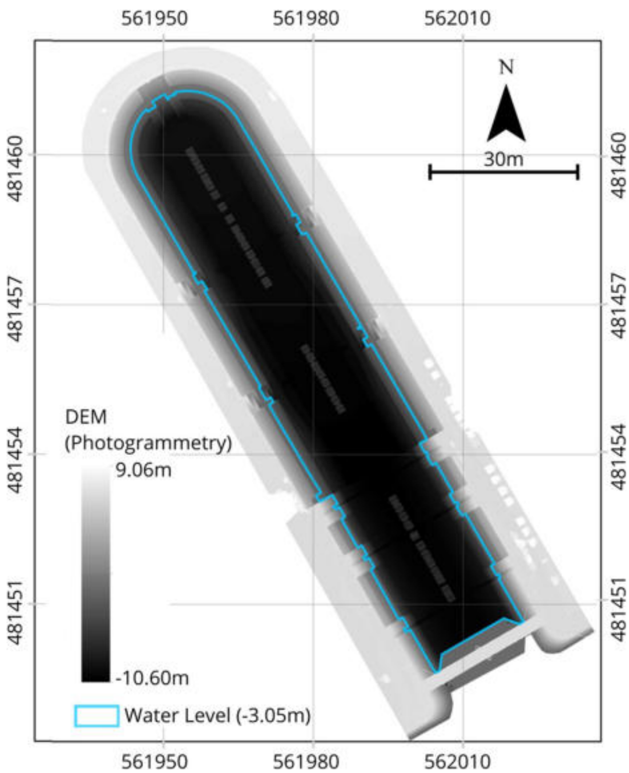

Fig. 4 DEM derived from UAV-based photogrammetric survey. The model represents the dock floor and sidewalls, with elevation values referenced to mean sea level (AMSL). The waterline (− 3.05 m AMSL) is also indicated for comparison

Monitoring (SHM) surveys and for planning targeted follow-up with higher-precision methods.

3 Results

3.1 Quality assessment of DAP-UAV checkpoints

The GSD of the photogrammetric survey was 0.55 cm, and the internal quality of the UAV photogrammetry (DAP-UAV) model is characterized by the RMSE of the GCP residuals (Table 3).

The low RMSE values obtained in all axes indicate high geospatial accuracy of the photogrammetric model, supporting its suitability as a reference surface for bathymetric validation in this study.

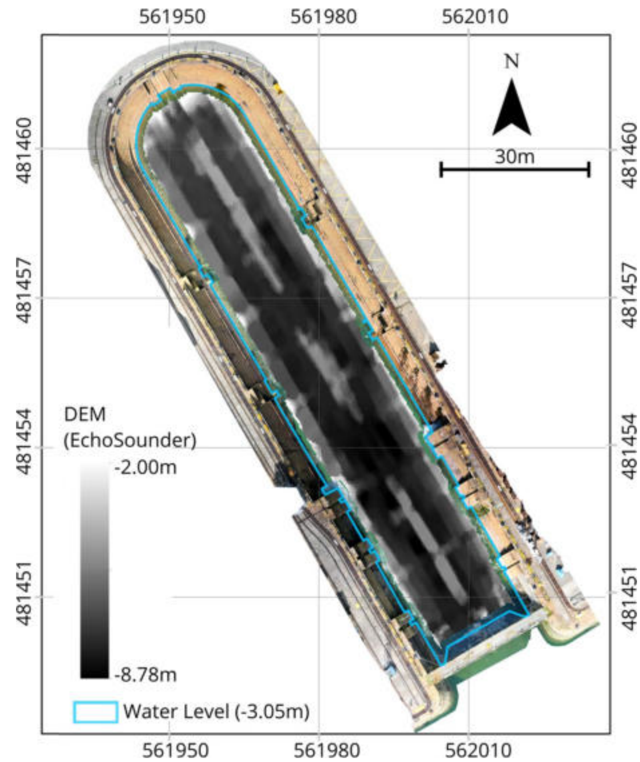

Fig. 5 DEM obtained from UAV-mounted single-beam echosounder survey. Depth values are referenced to mean sea level (AMSL)

3.2 Photogrammetric and Bathymetric Elevation Models

Photogrammetry generated a DEM, as shown in Fig. 4, with elevations ranging from approximately -10.60 m to 9.10 m. The surface representation demonstrates good accuracy, including detailed representations of the stepped sidewalls. This detailed modelling allows for a thorough analysis of elevation variations and facilitates the study of hard-to-reach areas, such as the contours and complex structures of the site.

The bathymetric DEM produced from the sonar survey is shown in Fig. 5. The sonar model is visualized in grayscale, with an orthophoto background added for contextual clarity. Elevations recorded by the sonar ranged from approximately − 9.33 m to − 2.55 m, reflecting exclusively submerged surfaces. This explains the difference in maximum elevation values compared to the photogrammetric DEM, which covered both submerged and dry areas.

3.3 Evaluation of the vertical accuracy of the sonar

The results of the comparison between the point clouds obtained by DAP-UAV and those acquired with the sonar are presented in Fig. 6.

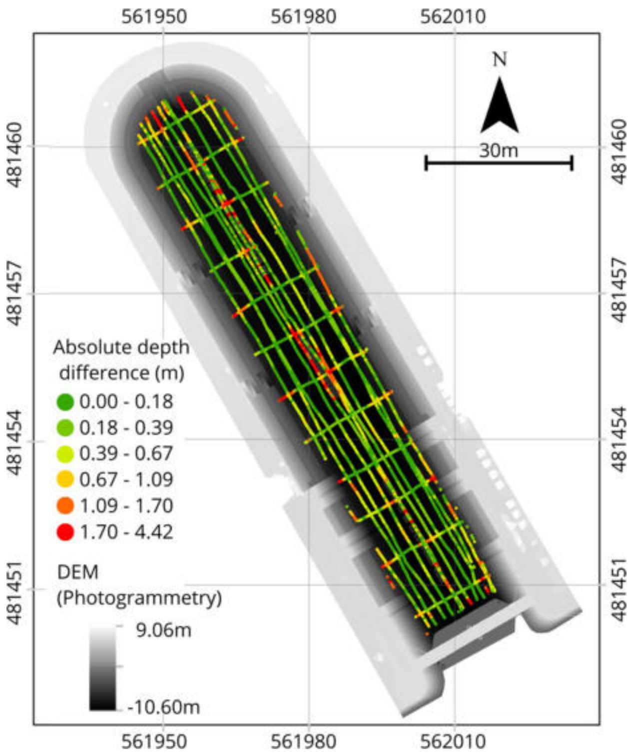

Fig. 6 Spatial distribution of absolute elevation differences between SBES measurements and photogrammetry-derived elevations (colour scale in metres). North arrow indicates map orientation

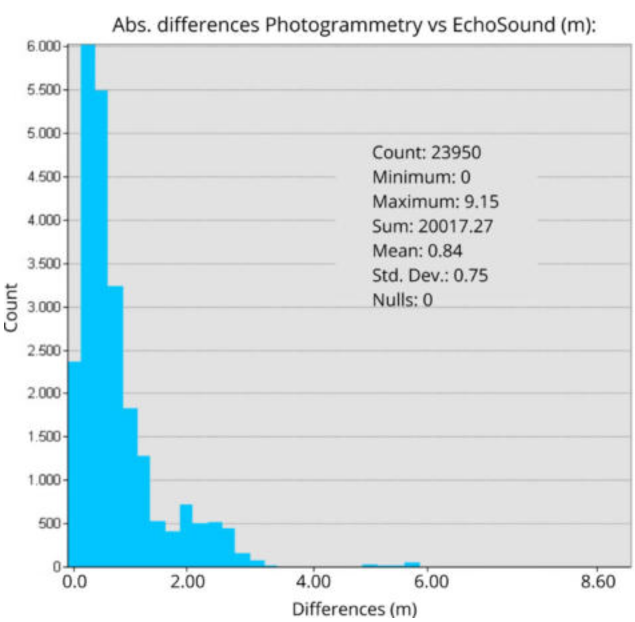

Fig. 7 Histogram of depth differences between the SBES and photogrammetry-derived elevations. Differences are shown in metres (SBES − photogrammetry). Sample size N = 16,137. Summary statistics: mean = 0.153 m; SD = 0.579 m; min = − 2.363 m; max = 4.416 m

The distribution of the differences between the elevation points measured by the sonar and those derived from photogrammetry is shown in Fig. 7. The analysis revealed a mean depth difference ($\Delta \bar{z}$) of 0.153 m and an RMSE of 0.579 m. The largest discrepancies were observed near the shorelines and in central areas containing wooden structures used for vessel support, which show complex, small-scale geometries that may have contributed to increased measurement variability.

3.4 Comparative profiles between photogrammetric and bathymetric models

To complement the evaluation of the vertical accuracy of the bathymetry obtained with the echosounder, longitudinal and transverse profiles were extracted in representative regions of the study area. These profiles were selected to cover different morphological conditions of the dock structure, such as sections with gentle slopes, deeper central areas, and regions with interference from physical structures, such as steps and wooden elements. Using DAP-UAV as a high-precision reference, the data obtained with the SBES were analysed along these sections, allowing a point-by-point assessment of elevation discrepancies. This approach not only facilitates the identification of systematic deviations in the bathymetric data but also enables a better understanding of error behaviour under varying topographic conditions. Figure 8 shows the location of the profiles within the dock area, including two transverse profiles and one longitudinal profile selected for this analysis.

The profiles encompass a range of morphological conditions (i.e., stepped walls, flat central channel areas, and wooden structures with irregular surfaces and fine details), allowing assessment of bathymetric performance in both simple and complex contexts. Graphical analysis shows that, in flat, unobstructed reaches, sonar measurements agree closely with the photogrammetric model, demonstrating its ability to capture bottom morphology when no abrupt variations are present. However, over steep terrain or complex features, the bathymetric DEM fails to reproduce the exact terrain geometry. In every profile, the sonar curve lies above the photogrammetric surface, highlighting its tendency to underestimate true depths. Although survey passes covered the dike flanks, the sonar failed to capture the steep margins. In shoreline profiles, photogrammetry clearly delineates the slope transition, whereas the sonar profile shows vertical gaps at the edges. These discrepancies concentrate in zones where the acoustic signal is attenuated, scattered, or subject to multiple reflections (particularly on vertical surfaces and protrusions), underscoring the sonar's limitations in low-reflectivity or intricately shaped environments. In poorly sampled marginal settings, the absence of data compromises

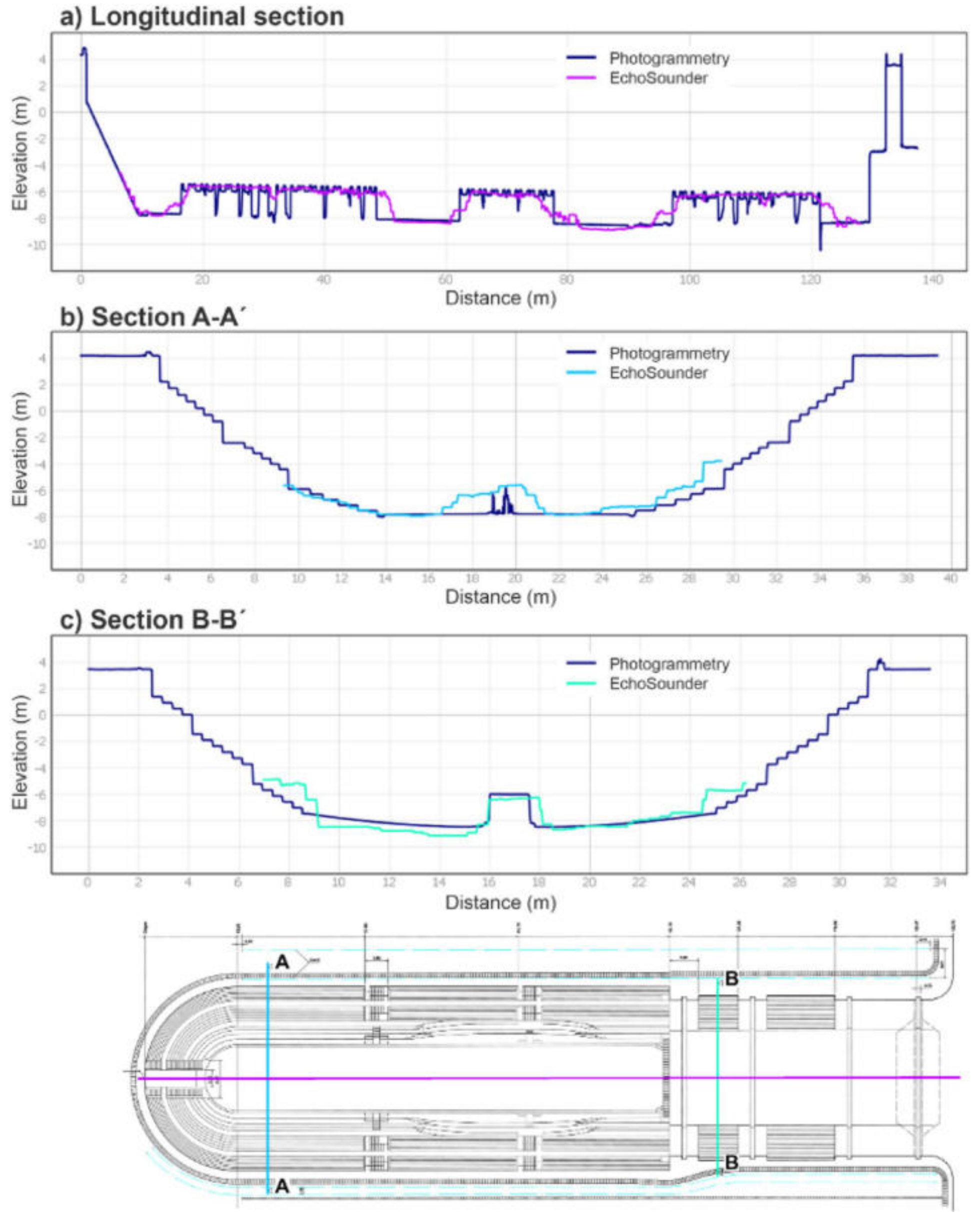

Fig. 8 Longitudinal and cross-sectional comparisons between photogrammetry and SBES measurements. **a** Longitudinal section along the dock showing photogrammetry-derived DEM (dark blue) and SBES points (magenta/cyan). **b** Cross-section A–A′ and **c** cross-section B–B′. Lower panel: plan view of the study dock indicating the location of the three profiles (A–A′ and B–B′) and the longitudinal transect. Image/processing credit: authors

complete bank mapping and reduces accuracy in volume calculations and habitat-zone delineation.

Figure 9 illustrates these discrepancies, represented by coloured points overlaid on the orthophoto, making it easier to visualize areas with greater altimetric variations. In general, the sonar measurements align better with the photogrammetry in areas with simpler relief. The largest discrepancies are observed in more complex zones, such as the margins and those with irregular surfaces, likely due to multipath reflections and signal scattering effects in these geometrically intricate environments.

4 Discussions

This study demonstrates that a UAV-mounted SBES system can reliably acquire bathymetric data in coastal infrastructure settings where traditional vessel-based surveys are impractical or unsafe, such as shallow zones, confined docks and narrow harbour channels. Suspending the transducer beneath a UAV provides excellent portability and rapid deployment, substantially reducing logistical overhead compared with boat-based campaigns.

Vertical accuracy analyses indicate close agreement between SBES and photogrammetric data in geometrically simple areas, showing that the system can effectively reproduce bottom morphology where surfaces are uniform and slopes are gentle. Conversely, discrepancies

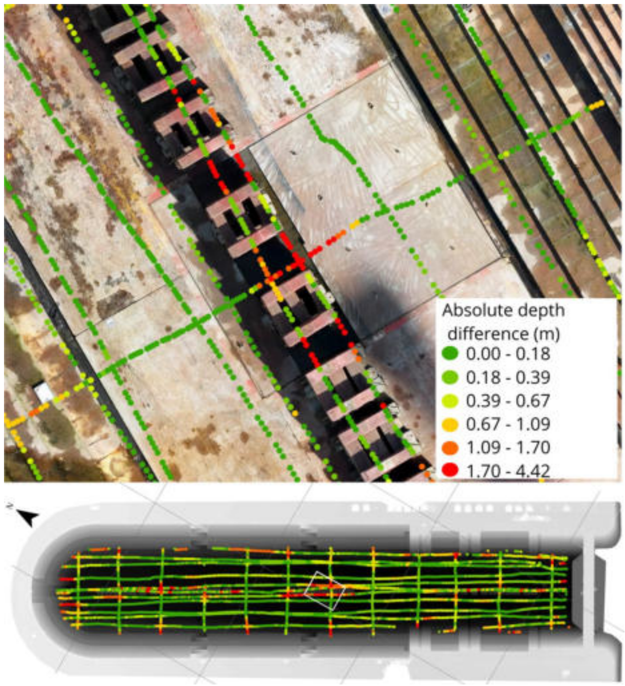

Fig. 9 Spatial distribution of depth differences (SBES − photogrammetry) over the study dock. Coloured dots indicate magnitude of absolute residuals in metres (legend). North arrow and scale bar shown

are concentrated near steep slopes, structural edges (e.g., stepped walls, wooden supports) and areas with unfavourable acoustic incidence, where signal attenuation, scattering and multipath reflections reduce measurement quality. A systematic tendency to underestimate depths near dock margins was also observed, reflecting an intrinsic limitation of nadir-oriented single-beam configurations for near-vertical or highly oblique surfaces.

Importantly, the novelty of this work lies in the combination of elements that are under-represented in the peer-reviewed UAV-SBES literature: (i) an engineered testbed, an operational dry dock that can be drained and filled, which reproduces the geometric complexity of coastal structures; (ii) a water-free, high-density validation against an ultra-high-resolution photogrammetric DEM (0.55 cm GSD), eliminating water-column uncertainties; and (iii) a large co-registered dataset (N = 16,137) to depths of ~ 15 m acquired under a repeatable transect protocol. Together these features enable a dense, objective assessment of geometric accuracy in a context directly relevant to coastal asset monitoring.

For the co-located dataset, the UAV-mounted SBES yielded a mean depth difference of 0.15 m and a standard deviation of 0.58 m relative to the photogrammetric reference, at average depths approaching 12–15 m, corresponding to an approximate relative error of 1.25%. These figures are broadly comparable to earlier SBES studies carried out in shallower or inland settings and demonstrate that UAV-SBES is operationally feasible at greater depths and in structurally complex environments.

For example, Diaz et al. [13] reported mean depth errors of approximately 21.6 cm using a boat-towed sonar in shallow water bodies under 3 m depth, while Tuno et al. [25] achieved a RMSE of 0.17 m when validating SBES measurements up to 4.3 m depth against total station data. Bandini et al. [14] evaluated a tethered UAV-operated SBES in inland waters up to 35 m deep, reporting an absolute RMSE of ~ 0.12 m after bias correction, corresponding to ~ 2.1% of actual depth. Our comparable accuracy, with a relative error lower than that of some previous studies, achieved under greater depths and complex structural conditions, highlights the operational feasibility and robustness of UAV-mounted SBES systems for preliminary bathymetric mapping beyond the shallow inland settings typical of prior research.

Our experiments were conducted under relatively calm and controlled conditions; consequently, the uncertainty metrics reported here (σ, MDC_{95}) represent the best-case scenario for calm water performance. No explicit sound-velocity profile (SVP) correction was applied during processing, consistent with the simplified operational configuration adopted in this study. In operational coastal environments, several physical mechanisms can degrade SBES performance and increase both random dispersion and systematic bias: (i) hydrodynamic motion, which disturbs UAV stability and transducer attitude and therefore introduces variable range errors and horizontal misalignment; (ii) water column effects, which attenuate and disperse acoustic energy and can alter travel times, producing signal-to-noise ratio loss and range bias; and (iii) acoustic and multipath interference, especially near vertical structures and vessel traffic, which can induce spurious echoes or temporally shifted returns. Although many SBES units operate in relatively high acoustic frequency ranges, interference is still possible in busy port environments, and multipath effects are exacerbated near hard, near-vertical boundaries.

4.1 Implications for structural health monitoring: detectability and operational integration

We position the UAV-mounted SBES workflow as a Level 1 (screening) tool within multi-level SHM strategies. To quantify detectability, we derived the MDC_{95} from the observed standard deviation (σ = 0.58 m) for single returns, resulting in $MDC_{95} \approx 1.61$ m. Averaging 11 returns reduces MDC_{95} to ≈ 0.49 m and averaging 65 returns to ≈ 0.20 m (Table X), for example. Thus, by designing transect geometry and flight plans to produce multiple colocalized samples (or repeating surveys), the UAV-SBES workflow can detect moderate bathymetric changes (decimetre scale) relevant for screening.

For operational integration into SHM programs, we recommend: (i) defining alarm thresholds based on the MDC and the context of the engineering decision (e.g., signalling if $\Delta z > 0.5$ m for $N \geq 11$ average samples); (ii) standardized transect geometry and flight kinematics to ensure footprint reproduction; (iii) periodic bias checks against a sparse set of surveyed control points or occasional ground soundings; (iv) rigorous metadata capture (flight logs, sonar settings, water/sound velocity profiles, weather) and data archiving to allow retrospective reprocessing; and (v) automatic routing rules that escalate signalled anomalies to Level 2 (MBES/directed total station) or Level 3 (detailed diagnostics) actions.

Repeatability was not experimentally evaluated in the present campaign; but it is technically feasible given the georeferenced acquisition (27 GCPs surveyed and RTK/PPK positioning).

With the calculation of MDC_{95}, it is possible to translate measurement uncertainty into operational criteria for structural health monitoring (SHM). In practical terms, this implies the following:

(i) Screening (Tier-1) in a single pass. With a single return, the MDC_{95} is relatively high, so the UAV-SBES system is particularly suitable for detecting changes of large magnitude, for example, metric-scale erosion, significant block displacement, vessel impacts, or large-amplitude settlements.
(ii) Improvement through replication. If the survey is designed to generate multiple colocalized returns (overlapping transects, reduced flight speed, or repeated passes), the detection threshold decreases by approximately $1/\sqrt{m}$. Thus, through replication and averaging of samples, the method can identify changes of moderate magnitude (decimetric scale), making it useful for detailed screening and prioritization of interventions.
(iii) Resolution limitations. The UAV-SBES is not suitable for SHM tasks requiring micrometre to millimetre resolution (e.g., monitoring of local cracks or deformations), which still require contact sensors (strain gauges, FBG) or high-precision ground-based methods.

4.2 Practical operational implications and mitigation strategies

Operational constraints meaningfully influence where and when UAV-mounted SBES surveys are feasible. Increased payload mass and external drag reduce flight endurance and therefore the areal coverage per sortie; added suspended mass and cable can produce pendulum motion that amplifies attitude variability under wind gusts, degrading depth precision. Although the acoustic sensor's raw data were recorded over a direct cable link to the onboard computer (minimising susceptibility to RF interference during acquisition), cable management is critical; poorly secured cables increase swing and risk connector ingress or damage.

To mitigate these effects we recommend conservative operational practices: plan missions in windows of low wind and no precipitation whenever possible; perform pre-flight payload/endurance tests and re-calculate achievable transect lengths for the loaded configuration; reduce flight speed and altitude (within safety margins) over critical survey lines to increase sample density and reduce pendulum motion; use robust cable routing, strain relief and waterproof connectors; keep spare batteries and limit individual sortie lengths to maintain a margin of safety. These measures reduce environmental and mechanical sources of uncertainty and should be adopted in any operational protocol derived from the present workflow.

The dry-dock experiment presented in this study should be interpreted as a metrological validation framework rather than an operational monitoring scenario. Its primary objective is to isolate and quantify the intrinsic performance of a UAV-mounted SBES system, eliminating water-column effects that typically confound underwater validation. While real-world SHM applications rarely provide access to absolute ground truth, the controlled environment enables the derivation of robust uncertainty metrics and minimum detectable change thresholds (e.g., MDC_{95}), which can subsequently inform the interpretation of measurements in practical deployments where validation relies on repeatability, sparse controls, or comparative surveys.

5 Conclusions

We evaluated a UAV-mounted single-beam echosounder (ECT400) for rapid bathymetric monitoring of coastal infrastructure in a controlled dry-dock test field. Our results showed that in flat and unobstructed areas, the SBES accurately reproduces bottom morphology with a precision comparable to UAV photogrammetry, demonstrating that UAV-SBES can deliver reliable depth information for preliminary surveys and routine screening in shallow and confined environments.

Although vertical precision does not match that of dedicated multibeam systems and local errors increase near steep or geometrically complex features, the UAV-SBES workflow offers a cost-effective, portable and safe option for frequent inspections and change detection. The co-located dataset produced a mean depth difference of 0.15 m (σ = 0.58 m). From this residual variability we derived a practical MDC_{95}: approximately 1.6 m for a single, co-located return

Table 4 Minimum Detectable Change at 95% confidence (MDC_{95}) for different numbers of averaged co-located sonar returns (m)

m (number of averaged co-located samples)	MDC_{95} (m)
1	1.61
5	0.72
11	0.49
65	0.20
259	0.10

and approximately 0.5 m when about 11 co-located returns are aggregated (Table 4). Consequently, the method is best framed as a Tier-1 screening tool, appropriate for detecting metre-scale changes (major scour, block displacement, vessel impacts) in single-pass surveys and decimetre-scale changes when survey designs deliberately replicate measurements (overlapping transects, reduced speed, repeated passes) and aggregate results. It is not suitable for SHM tasks requiring millimetre-to-sub-millimetre resolution, like crack propagation or fine deformation, which remain the domain of contact sensors (strain gauges, FBG) or high-precision terrestrial methods.

Operationally, we recommend the following monitoring strategy: (i) use rapid UAV-SBES surveys for high-temporal-frequency screening; (ii) define empirical detection thresholds from site-specific σ and desired MDC and plan transect spacing and repetition; accordingly, (iii) trigger targeted Tier-2 follow-up investigations when changes exceed those thresholds. Limitations that must be considered before operational deployment include environmental effects, platform constraints, and material-dependent acoustic responses; we discuss mitigation measures in the Discussion.

Future research should concentrate on quantifying repeatability across multiple campaigns, integrating sound-speed profiling for acoustic correction, testing alternative transducer configurations and developing automated change-detection routines that are fit for operational SHM. Further work should also expand validation to other material types, diverse hydrodynamic regimes (open ocean wave action, estuarine currents), and varying water qualities, as well as comparing performance across platforms. Such studies will quantify material- and environment-dependent biases and broaden the applicability of the workflow to a wider range of real-world monitoring scenarios.

Supplementary Information The online version contains supplementary material available at https://doi.org/10.1007/s13349-026-01086-1.

Acknowledgements The authors would like to thank the Chief and personnel of the Naval Arsenal of Ferrol for allowing us to use the Dique de la Campana and for all the facilities and help provided to complete this work. We thank Rocío López Juanes for her collaboration in the tasks of the study.

Author contributions Bethsaide Souza Santos: Investigation, Methodology, Writing – Original Draft. Marcos Arza-García: Data curation; Formal analysis; Validation; Visualization; Writing — review & editing. Juan Ortiz-Sanz: Conceptualization, Formal Analysis, Supervision, Writing – Review & Editing. M. Luz Gil-Docampo: Conceptualization, Funding Acquisition, Resources, Supervision.

Funding The Article Processing Charge (APC) for the publication of this research was funded by the Coordenação de Aperfeiçoamento de Pessoal de Nível Superior - Brasil (CAPES) (ROR identifier: 00x0ma614). This work was supported in part by the European Commission, through the grant POCTEP-INTERREG, 0054_AEROGANP_1_E; This work is also funded by the Xunta de Galicia, Spain, with a postdoctoral fellowship awarded to Marcos Arza García (ED481D-2025/003) and it was also possible thanks to the Brazilian Government through the State University of Feira de Santana, which granted paid leave to Bethsaide Souza Santos.

Data availability The datasets generated and analysed during the current study are available from the corresponding author on reasonable request.

Declarations

Conflict of interest The authors declare that they have no competing interests.

Open Access This article is licensed under a Creative Commons Attribution 4.0 International License, which permits use, sharing, adaptation, distribution and reproduction in any medium or format, as long as you give appropriate credit to the original author(s) and the source, provide a link to the Creative Commons licence, and indicate if changes were made. The images or other third party material in this article are included in the article's Creative Commons licence, unless indicated otherwise in a credit line to the material. If material is not included in the article's Creative Commons licence and your intended use is not permitted by statutory regulation or exceeds the permitted use, you will need to obtain permission directly from the copyright holder. To view a copy of this licence, visit http://creativecommons.org/licenses/by/4.0/.

References

1. Chen D, Wang Y, Huang H, Chen C, Yuan C (2017) A behavior-oriented formula to predict coastal bathymetry evolution caused by coastal engineering. Cont Shelf Res 135:47–57. https://doi.org/10.1016/j.csr.2017.01.013
2. Stevens AW, Moritz HR, Elias EPL, Gelfenbaum GR, Ruggiero PR, Pearson SG, McMillan JM, Kaminsky GM (2023) Monitoring and modeling dispersal of a submerged nearshore berm at the mouth of the Columbia River, USA. Coast Eng. https://doi.org/10.1016/j.coastaleng.2023.104285
3. Álvarez M, Carballo R, Ramos V, Iglesias G (2017) An integrated approach for the planning of dredging operations in estuaries. Ocean Eng 140:73–83. https://doi.org/10.1016/j.oceaneng.2017.05.014
4. Kim H, Lee SB, Min KS (2017) Shoreline change analysis using airborne LiDAR bathymetry for coastal monitoring. J Coast Res 33(Special Issue 79):269–273. https://doi.org/10.2112/SI79-055.1
5. Guo K, Xu W, Liu Y, He X, Tian Z, Xi C, Jiang R, District N (2017) Gaussian half-wavelength progressive decomposition method for waveform processing of airborne laser bathymetry. Remote Sens 10(1):35. https://doi.org/10.3390/rs10010035

6. Guo K, Li Q, Wang C, Mao Q, Liu Y, Zhu J, Wu A (2022) Development of a single-wavelength airborne bathymetric LiDAR: system design and data processing. ISPRS J Photogramm Remote Sens 185:62–84. https://doi.org/10.1016/J.ISPRSJPRS.2022.01.011
7. Cao B, Deng R, Xu Y, Cao B, Liu Y, Zhu S (2022) Practical differences between photogrammetric bathymetry and physics-based bathymetry. IEEE Geosci Remote Sens Lett. https://doi.org/10.1109/LGRS.2021.3095963
8. Misra A, Ramakrishnan B (2020) Assessment of coastal geomorphological changes using multi-temporal Satellite-Derived Bathymetry. Cont Shelf Res 207:104213. https://doi.org/10.1016/j.csr.2020.104213
9. Yang F, Bu X, Ma Y, Lu X, Wang M, Shi B (2017) Geometric calibration of multibeam bathymetric data using an improved sound velocity model and laser tie points for BoMMS. Ocean Eng 145:230–236. https://doi.org/10.1016/j.oceaneng.2017.09.010
10. Zhou J, Koge H, Maki T (2024) Automation of MBES noise reduction: an approach based on seafloor bathymetry features derived from manual editing procedures. Ocean Eng. https://doi.org/10.1016/j.oceaneng.2024.117397
11. Tripathi J, Murphy RR (2023) Using an uncrewed surface vehicle to create a volumetric model of non-navigable rivers and other shallow bodies of water. arXiv:2309.10269
12. Hatanaka K, Toda M, Wada M (2008) Data analysis of a low-cost bathymetry system using fishing echo sounders. In: Proceedings of OCEANS 2007 MTS/IEEE conference; 2007 Oct 29–Nov 1; Vancouver, BC. IEEE. https://doi.org/10.1109/OCEANS.2007.4449181
13. Diaz AL, Ortega AE, Tingle H, Pulido A, Cordero O, Nelson M, Cocoves NE, Shin J, Carthy RR, Wilkinson BE, Ifju PG (2022) The Bathy-Drone: an autonomous uncrewed drone-tethered sonar system. Drones. https://doi.org/10.3390/drones6100294
14. Bandini F, Olesen D, Jakobsen J, Kittel CMM, Wang S, Garcia M, Bauer-Gottwein P (2018) Technical note: bathymetry observations of inland water bodies using a tethered single-beam sonar controlled by an unmanned aerial vehicle. Hydrol Earth Syst Sci 22(8):4165–4181. https://doi.org/10.5194/hess-22-4165-2018
15. Mopin I, Marchal J, Legris M, Chenadec GL, Blondel P, Zerr B (2022) Design and field testing of a non-linear single-beam echosounder for multi-frequency seabed characterization. Appl Acoust. https://doi.org/10.1016/j.apacoust.2021.108490
16. Ri US, Rim UR, Jong GC (2025) Estimation of single-beam echo sounder signal for riverbed classification. Mar Syst Ocean Technol. https://doi.org/10.1007/s40868-024-00154-9
17. Gogendeau P, Bonhommeau S, Fourati H, Julien M, Contini M, Chevrier T, Nieblas AE, Bernard S (2025) An autonomous surface vehicle for acoustic tracking, bathymetric and photogrammetric surveys. Ocean Eng 331:121201. https://doi.org/10.1016/j.oceaneng.2025.121201
18. Mirzazade A, Popescu C, Gonzalez-Libreros J et al (2023) Semi-autonomous inspection for concrete structures using digital models and a hybrid approach based on deep learning and photogrammetry. J Civ Struct Health Monit 13(8):1633–1652. https://doi.org/10.1007/s13349-023-00680-x
19. Wang J, Ueda T, Wang P et al (2025) Building damage inspection method using UAV-based data acquisition and deep learning-based crack detection. J Civ Struct Health Monit. https://doi.org/10.1007/s13349-024-00836-3
20. Khomsin, Pratomo DG, Saputro I (2021) Comparative analysis of singlebeam and multibeam echosounder bathymetric data. In: IOP conference series: materials science and engineering, vol 1052, p 012015. https://doi.org/10.1088/1757-899x/1052/1/012015
21. Ni H, Wang W, Ren Q, Lu L, Wu J, Ma L (2019) Comparison of single-beam and multibeam sonar systems for sediment characterization: results from shallow water experiment. In: IEEE Seattle, Oceans. https://doi.org/10.23919/OCEANS40490.2019.8962802
22. Linton-Izquierdo C, Salas-Monreal D, Athie G, Ake-Castillo JA, Marín-Hernandez M, de Guadalupe Bernal-Ramírez R (2024) Turbidity estimation from an acoustic backscatter signal in a tropical coral reef system. Estuar Coast Shelf Sci. https://doi.org/10.1016/j.ecss.2024.109018
23. Mohammadloo TH, Snellen M, Renoud W, Beaudoin J, Simons DG (2019) Correcting multibeam echosounder bathymetric measurements for errors induced by inaccurate water column sound speeds. IEEE Access 7:122052–122068. https://doi.org/10.1109/ACCESS.2019.2936170
24. Praet N, Collart T, Ollevier A, Roche M, Degrendele K, De Rijcke M, Urban P, Vandorpe T (2023) The potential of multibeam sonars as 3D turbidity and SPM monitoring tool in the North Sea. Remote Sens 15(20):4918. https://doi.org/10.3390/rs15204918
25. Tuno N, Kulo N, Perić D, Đidelija M, Hamzić A, Topoljak J, Mulahusić A, Kogoj D (2024) Analyzing depth uncertainty of near-shore bathymetric survey conducted by single-beam echo sounder. Teh Glas 18:84–91. https://doi.org/10.31803/tg-20241008141610
26. Chen C, Zheng H, Tian W, Wang Z, Li H (2021) Detection method for single-beam echo sounder based on equivalent measurement. In: Journal of physics: conference series, vol 1739, p 012021. https://doi.org/10.1088/1742-6596/1739/1/012021
27. Kartal SK, Hacıoğlu R, Görmüş KS, Kutoğlu H, Leblebicioğlu MK (2022) Modeling and analysis of sea-surface vehicle system for underwater mapping using single-beam echosounder. J Mar Sci Eng 10(10):1349. https://doi.org/10.3390/jmse10101349
28. Famiglietti NA, Miele P, Memmolo A, Moschillo R, Migliazza R, Vicari A (2025) Bathymetry reconstruction using UAV-mounted echo-sounder and lidar sensors: a case study. Rend Online Soc Geol Ital 66:63–70. https://doi.org/10.3301/ROL.2025.12
29. Alamillo AA, Círculo D, Español N (2001) Los diques secos del arsenal de ferrol: realidades y proyectos

Publisher's note Springer Nature remains neutral with regard to jurisdictional claims in published maps and institutional affiliations.